Proceedings of the 11th World Congress on Mechanical, Chemical, and Material Engineering (MCM'25)

Paris, France - August, 2025 Paper No. HTFF 251 DOI: 10.11159/htff25.251

# Numerical Analysis of Pulsed Electric Field Effects on Droplet Dynamics in Electrostatic Rotary Bell Spraying

## Amine Benmoussa<sup>1\*</sup>, Mohammad-Reza Pendar<sup>2</sup>, José Carlos Páscoa<sup>1</sup>

<sup>1</sup>University of Beira Interior, Center for Mechanical and Aerospace Science and Technologies (C-MAST),
Calçada Fonte do Lameiro, 6201-001 Covilhã, Portugal
amine.benmoussa@ubi.pt; pascoa@ubi.pt

<sup>2</sup>University of Victoria, Department of Mechanical Engineering
British Columbia V8W2Y2 Victoria, Canada
pendar@uvic.ca

**Abstract** – This study presents a comprehensive 3D Eulerian-Lagrangian analysis of droplet behavior in an electrostatic rotary bell sprayer operating under pulsed electric fields. The simulations are performed using OpenFOAM, incorporating a Large Eddy Simulation (LES) turbulence model to capture the complex, high-Reynolds-number airflow typical of industrial spray system, along with spray dynamics, electric field modeling, and droplet tracking. The results highlight how pulsed voltage parameters influence droplet dispersion patterns, transfer efficiency and coating uniformity. These findings offer new insights for optimizing electrostatic spray technologies and demonstrate the potential of pulsating electric fields to improve energy efficiency and coating performance in automotive and other industrial applications.

Keywords: Electrostatic spraying, Large Eddy Simulation, Pulsed voltage, Droplet dynamics, Particle charging, OpenFOAM

#### 1. Introduction

Electrostatic spray painting has become widely adopted technique in automotive and aerospace industries due to its high transfer efficiency, reduced overspray, and uniform coating quality. At the core of this technology lies the electrostatic rotary bell sprayer (ERBS) that atomizes paint into a fine spray of charged droplets using a rapidly spinning bell-cup and high-voltage electric fields. The centrifugal forces generated by the bell-cup stretch the paint into ligaments along its inner surface, which then break into droplets, while shaping air guides the spray toward the target. An electric field between the bell and the grounded surface further improves transfer efficiency by attracting the charged droplets for better coating coverage [1]. This technique enables precise deposition of material even on complex geometries, making it essential in modern coating processes.

Recent advances in electrostatic spray technologies have improved understanding of droplet transport, space charge effects [2], droplet size distributions [3], and airflow shaping for spray effectiveness [4]. Numerical simulations have played a key role in these efforts; Im et al. [5] applied CFD to investigate the transfer process in electrostatic rotary bell sprayers. According to them, charge-to-mass ratio, electrostatic forces, and transfer efficiency are extremely sensitive to conductor geometry and applied voltage. They further stated that increasing the shaping airflow could reduce transfer efficiency; this reflects the tight optimum necessary when adjusting the parameters of the spray. Yasumura et al. [6] investigated high-speed rotary bell cups and found that both the applied voltage and shaping airflow significantly influenced droplet size distributions, stressing the combined roles of electrostatic and aerodynamic effects in determining atomization outcomes. Further emphasizing electrostatic effects. Pendar and Páscoa [7, 8] studied the flow field and particle charging dynamics in electrostatic spraying alongside a voltage applied conductor geometry which they said decisively influences the spray characteristics. Colbert et al. [9], through parametric analysis, reported material build-up along target edges when employing ring-shaped spray patterns—an observation that underscores the challenge of achieving uniform deposition with conventional configurations. Krishna et al. [10], using three-dimensional simulations, studied near-bell atomization with a focus on electrohydrodynamic (EHD) phenomena. They found that electric forces promote the formation of finer droplets without disrupting primary atomization. Toljic et al. [11] performed numerical analyses to evaluate how variations in the electric charge carried by paint droplets influence the spray mass flux directed toward the target surface. Oswald et al. [12] explored how elongational resistance influences droplet breakup in rotary bell systems, offering a deeper understanding of fluid deformation during atomization. Shen et al. [13] contributed further by simulating droplet disintegration and the flow

behavior of non-Newtonian paints [14, 15] in high-speed rotary bell sprayers. Recently, Krishna and Owkes [16] examined atomization in ERBS configurations and demonstrated how electric fields play a pivotal role in droplet breakup. The results supported how droplet size, charge distribution, and breakup dynamics are very sensitive to electrostatic forces and provide important information for optimizing TE in industrial systems.

While prior research on electrostatic rotary bell sprayers (ERBS) has examined droplet behaviour and transfer efficiency under constant voltage [17], the role of pulsed electric fields in shaping spray characteristics remains largely unexplored. In the present work, we study the influence of pulsating voltages on electrostatic spray performance in ERBS systems equipped with a control ring across various operations. Using a 3D Eulerian-Lagrangian framework in OpenFOAM and LES turbulence model, the simulations capture detailed interactions between electric fields, airflow, and droplet dynamics. The results provide new perspectives on how voltage modulation affects charge distribution, droplet paths, and deposition efficiency.

## 2. Governing Equations

#### 2.1 Continuous Phase

The airflow is governed by the compressible Navier-Stokes equations coupled with a Large Eddy Simulation (LES) turbulence model. LES captures large-scale turbulent structures while modeling the smaller sub-grid effects. This is achieved through Favre filtering, where flow variables are split into resolved grid-scale (GS) and unresolved sub-grid (SGS) components using a filter function  $G = G(X, \Delta)$ , with  $\Delta = \Delta(X)$  representing the local filter width [18, 19].

The filtered continuity and momentum equations are:

$$\frac{\partial \bar{\rho}}{\partial t} + \frac{\partial (\bar{\rho} \ \bar{u}_j)}{\partial x_i} = 0,\tag{1}$$

$$\frac{\partial \bar{\rho}}{\partial t} + \frac{\partial (\bar{\rho} \, \bar{u}_j)}{\partial x_j} = 0,$$

$$\frac{\partial (\bar{\rho} \bar{u}_j)}{\partial t} + \frac{\partial (\bar{\rho} \bar{u}_i \bar{u}_j)}{\partial x_j} = -\frac{\partial \bar{\rho}}{\partial x_i} + \frac{\partial \bar{\sigma}_{ij}}{\partial x_j} - \frac{\partial \tau_{ij}}{\partial x_j} + f_{st} + f_{es} + S.$$
(2)

The viscous stress tensor  $\tilde{\sigma}_{ij}$ , is given by:

$$\tilde{\sigma}_{ij} = \bar{\mu} \left( \frac{\partial \tilde{u}_i}{\partial x_i} + \frac{\partial \tilde{u}_j}{\partial x_i} - \frac{2}{3} \delta_{ij} \frac{\partial \tilde{u}_k}{\partial x_k} \right), \tag{3}$$

Here, p,  $\bar{\mu}$  and  $\delta_{ij}$  are the pressure, the kinematic viscosity and the Kronecker delta function, respectively. The electric stress  $(f_{es})$ , surface tension  $(f_{st})$  and gravity (S) are included to represent physical interactions in the spray process. The SGS stress tensor,  $\tau_{ij}$ , can be decomposed as [20]:

$$\tau_{ij} \approx \bar{\rho}(\overline{u_i u_j} - \overline{u_i u_j}) , \qquad (4)$$

#### 2.2 Electric Field

The electric field is created by the voltage difference between the negatively charged droplets and the grounded target. It is computed by solving Poisson's equation, more details are provided in our previous work [18]:

$$\nabla^2 \varphi = -\frac{\rho^q}{\varepsilon'} \,. \tag{5}$$

where  $\rho^q$  is the space charge density and  $\varepsilon'$  is air permittivity. The electric field  $(\vec{E})$  and charge of each particle  $(q_{P_i})$ are calculated by:

$$\vec{E} = -\nabla \varphi , \varepsilon' \nabla . E = \rho^q , \tag{6}$$

$$q_{P_i} = m_{P_i} \, \rho_{m_i}^q = (\rho_P V_{P_i}) \rho_{m_i}^q, \tag{7}$$

with  $\rho_P$ ,  $V_{P_i}$ , and  $\rho_{m_i}^q$  denoting the density, droplet volume, and charge to mass ratio, respectively. The resulting electrostatic force  $(F_E)$  acting on each droplet is:

$$F_E = q_{P_i} E = m_{P_i} \rho_{m_i}^q E \,, \tag{8}$$

where  $m_{P_i}$  and  $q_{P_i}$  are the mass and the charge of each individual droplet, respectively.

### 2.3 Discrete Phase

Droplets are tracked in airflow using a Lagrangian framework by solving differential equations and applying Newton's law for force balances. The forces affecting droplet trajectory—Stokes drag  $(f_D)$ , electric force  $(f_E)$ , gravity  $(f_G)$ , and added-

$$\vec{F}_{P} = m_{p} \frac{\partial \vec{u}_{p}}{\partial t} = \frac{3}{4} C_{d} \frac{\rho_{f}}{\rho_{P}} \frac{m_{P}}{2R_{P}} \left| (\vec{u}_{f} - \vec{u}_{P}) \right| (\vec{u}_{f} - \vec{u}_{P}) + (\rho_{P} - \rho_{f}) V_{P} \vec{g} + \vec{E} q_{P} + \frac{\rho_{f} V_{P}}{2} \frac{\partial (\vec{u}_{f} - \vec{u}_{p})}{\partial t}$$
(9)

Where  $\vec{u}_P$  and  $\vec{u}_f$  are the particles and fluid velocity vectors,  $\rho_P$  and  $\rho_f$  represent the densities of particles and fluid, respectively.  $q_P$ ,  $m_P$ ,  $V_P$  and  $R_P$  correspond to the charge, mass, volume and radius of the particles, respectively.

The drag coefficient (
$$C_D$$
) depends on the particle's Reynolds number ( $Re_p = \frac{2R_P |\vec{u}_f - \vec{u}_p| \rho_f}{\mu_f}$ ), and is given by [18, 19]:
$$C_D = \begin{cases} 24/Re_P, & \text{if } Re_P < 1\\ (24/Re_P) (1 + 0.5 Re_P^{0.687}), & \text{if } 1 \le Re_P \le 1000\\ 0.44, & \text{if } Re_P > 1000 \end{cases}$$
(10)

Whith  $\vec{\mu}_f$  denote the air dynamic visco

## 2.4 Breakup Model:

Spraying involves two breaking up stages. The primary breakup involves the initial liquid disintegration into droplets as it exits the nozzle, described by the Rosin-Rammler distribution  $(Y_d = exp(\frac{-d}{\overline{d}})^n)$ . During secondary breakup: Larger droplets break further into smaller ones, modeled using the Taylor Analogy Breakup (TAB) approach. This model uses the Weber number  $(We = \frac{\rho u_{rel}^2 D_P}{2})$  to predict breakup of parent droplets based on the product generation rate dn(t)/dt and a proportional constant  $(K_{br})$ , given by:

$$\frac{dn(t)}{dt} = -3K_{br}n(t),\tag{11}$$

$$K_{br} = \begin{cases} k_1 \omega & \text{if } We \leq We_t \\ k_2 \omega \sqrt{We} & \text{if } We > We_t. \end{cases}$$

$$(11)$$

With  $We_t$  is set to 100, and  $k_1 \approx k_2 = 0.2$  to match experimental droplet size and velocity [8]. The resultant product oplet distribution is: droplet distribution is:

$$\frac{r_{pr}}{r_{na}} = e^{-K_{br}t} \tag{13}$$

Where  $r_{pa}$  and  $r_{pr}$  represent the parent and product droplets radius.

## 3. Electrospray Characteristic and Boundary Conditions

The computational domain and boundary conditions are shown in Fig. 1, were designed to replicate the operation of a rotary bell-type electrostatic sprayer (ERBS) fitted with a control ring. The bell cup of D=65 mm diameter is centered in a cylindrical domain, serving as the reference scale (D) for all dimensions. The ring conductor measures 4.6D in diameter. The domain itself spans 40D in diameter and 12D in height, ensuring sufficient flow development. A circular target (22D diameter) is placed 3.8D downstream of the bell. The bell rotates at 30krpm and high-pressure shaping air exits at 150 norm. l/min. Inlet flow is set at 0.2 m/s to mimic paint booth downdraft. No-slip conditions are applied to all walls, with a moving wall boundary for the rotating bell. Electrostatic potentials are applied to the stainless-steel components (bell, ring, collar),

while non-conductive parts are modeled with zero normal gradient (( $\nabla \Phi$ ). n = 0). The other boundaries are grounded ( $\Phi$  = 0), with charge ( $\rho_{\rm m}^{\rm q}$ ) of -0.5 mC/kg is assigned to atomized droplets.

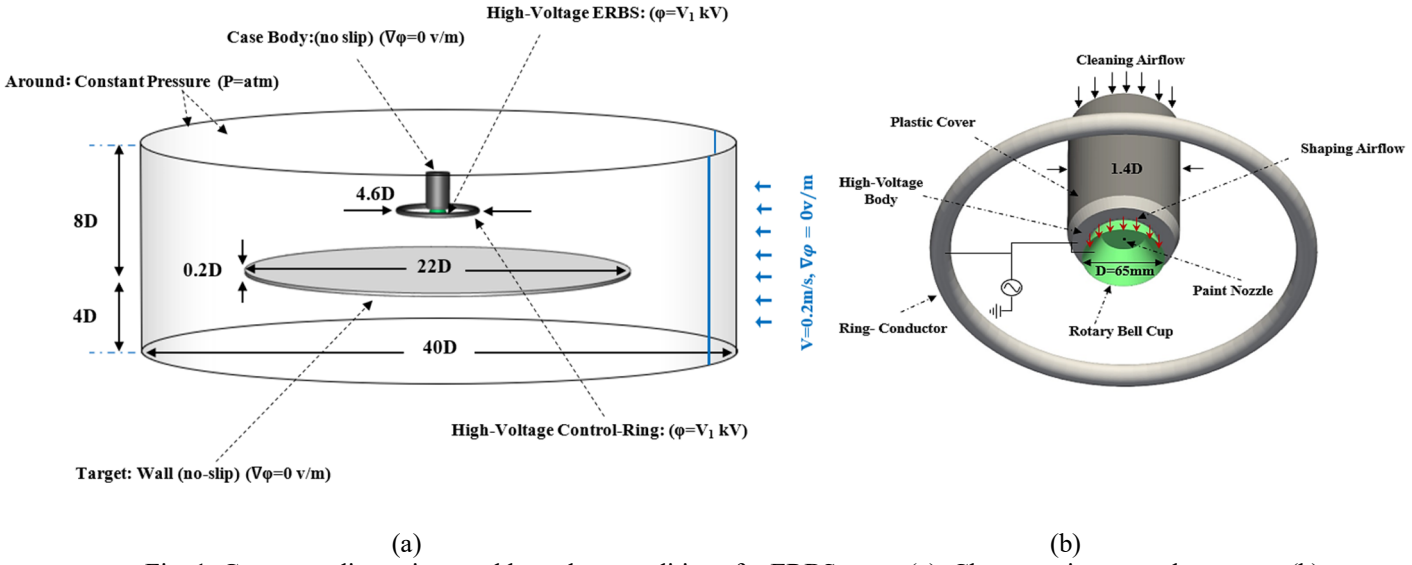


Fig. 1. Geometry dimensions and boundary conditions for ERBS spray (a). Close-up view near the sprayer (b).

Figure 2 presents a 3D view of the structured quadrilateral mesh used for the entire domain, consisting of 8.5 million cells based on our earlier work [18]. It includes the full computational domain (Fig. 2a) and the sprayer cup with a high-voltage control ring (Fig. 2b). The mesh features a  $1.4\times10^{-4}$  m prism layer at solid surfaces, maintaining y<sup>+</sup> below 0.35. The simulation time step is set to  $1\times10^{-7}$  s.

In this study, we use second-order accurate discretization schemes and set a convergence criterion of  $1 \times 10^{-6}$  to ensure reliable results. The PIMPLE algorithm, which combines the strengths of PISO and SIMPLE, helps achieve stable and fast convergence even with larger time steps. In the Eulerian-Lagrangian simulation, wall treatment in LES turbulence modeling within OpenFOAM is based on the dimensionless wall distance  $(y^+ = (u_\tau . \Delta y)/v)$ , which depends on the friction velocity  $(u_\tau)$ , kinematic viscosity (v), and the distance to the wall  $(\Delta y)$  more details are provided in our previous work [18].

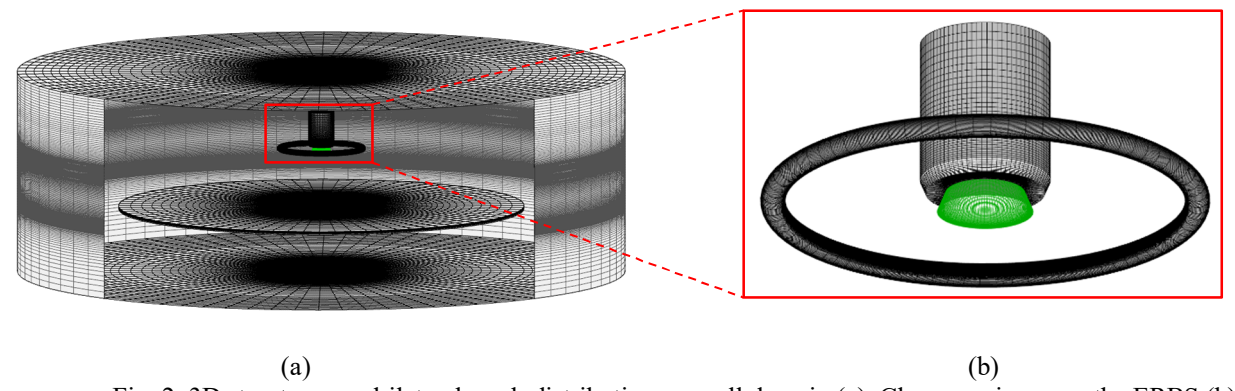


Fig. 2. 3D structure quadrilateral mesh distribution: overall domain (a). Close-up view near the ERBS (b).

### 4. Results and discussion

To verify our model, figure 3 presents a comparison of our simulation results with experimental data on air flow around the bell cup. The velocity profiles show strong agreement with the experimental results reported by Stevenin et al. [5], with discrepancies of less than 1.5%.

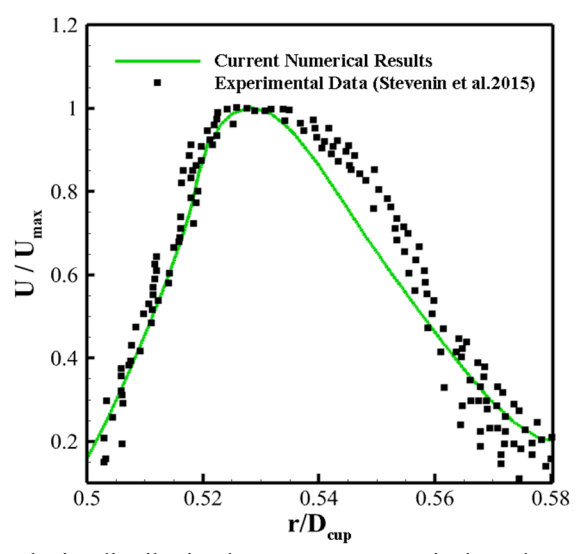


Fig. 3. Comparison of radial velocity distribution between our numerical results and experimental data [5].

Figure 4 displays the electric potential between the ERBS with the control ring and the target for constant voltage at -40 kV, as obtained from our CFD simulation. The contours show broader coverage areas with a stronger potential distribution across the computational domain, which influences spray patterns and droplet trajectories to accelerate the droplet transfer process. The negative voltage absolute value significantly helps to control the spray plume.

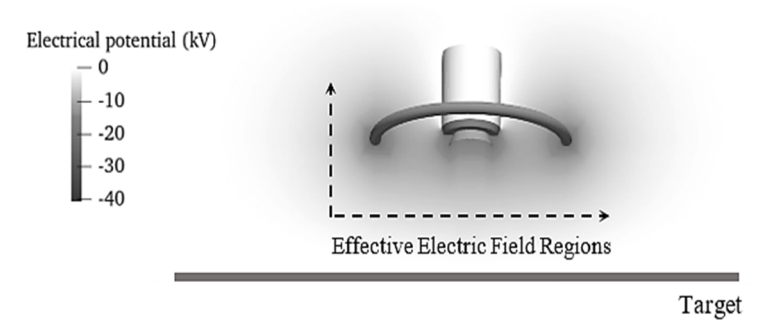


Fig. 4. Electrical field distribution around ERBS with control ring for constant voltage ( $V_{Cup} = -40 \ kV$ ,  $V_{Ring} = -40 \ kV$ ).

Figure 5 illustrates the influence of electric fields generated by constant and pulsed voltages at varying frequencies (200 Hz, 800 Hz, and 1600 Hz) on flow velocity streamlines, visualized using the Line Integral Convolution (LIC) method. In the baseline case (a), both the bell cup and control ring are maintained at a constant -40 kV. For pulsed cases, the bell cup voltage ranges between 0 kV and -40 kV<sub>rms</sub> while the control ring remains at -40 kV. At 200 Hz (Fig. 5b), the velocity filed displays a more rectangular shape at the plume's shoulder with increased instability patterns. The inner toroidal recirculation zone ( $R_{ln}$ ) is slightly diminished, while the outer toroidal recirculation zone ( $R_{out}$ ) pushes the spray shoulder outward, creating a more open angle. Increasing the frequency to 800 Hz (Fig. 5c) leads to better vortex breakdown behavior, producing a plume with a narrower shoulder and a smaller angle. At 1600 Hz (Fig. 5d), the flow structure is similar to that

at 800 Hz, though additional vortices and turbulent features emerge at the higher frequency. These results highlight how pulsed voltage alters velocity distribution, particularly in shaping the spray plume's shoulder.

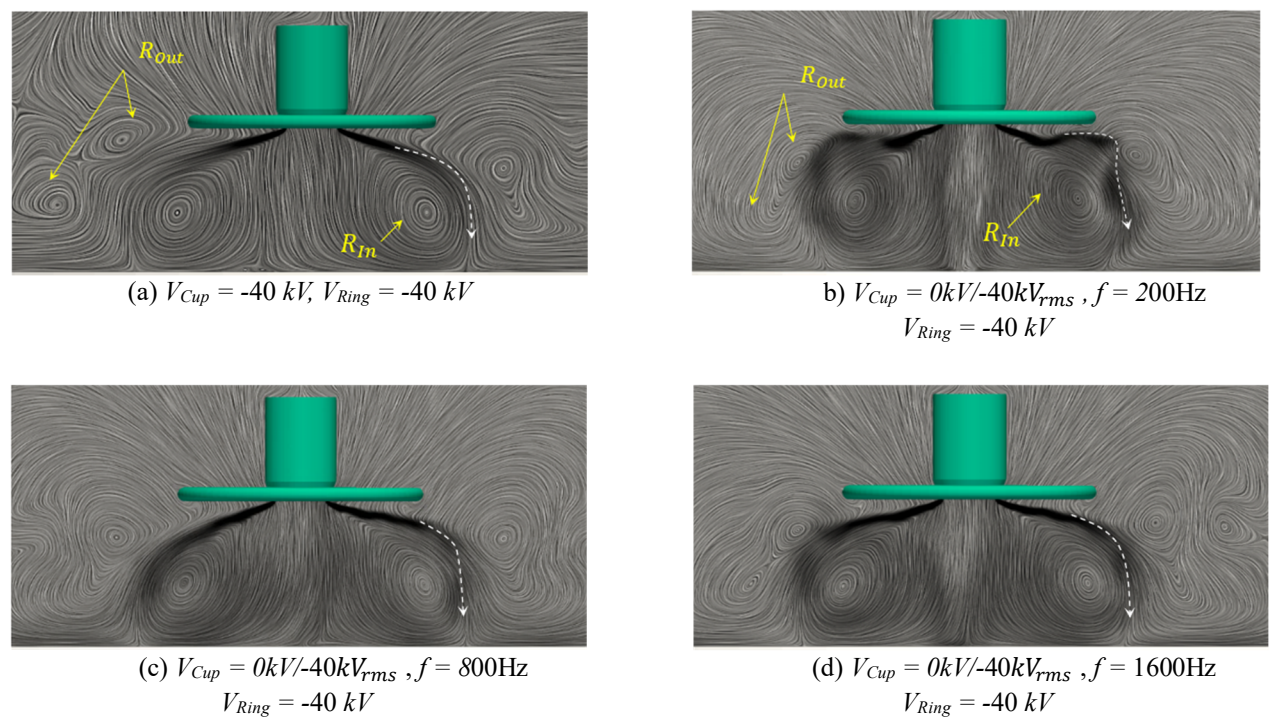


Fig. 5. Velocity field with streamlines comparison under constant constant voltage ( $V_{Cup} = -40 \ kV$ ,  $V_{Ring} = -40 \ kV$ ) and pulsed voltage applied to the sprayer's body cup ( $V_{Cup} = 0kV/-40 \ kV_{rms}$ ,  $V_{Ring} = -40 \ kV$ ) at different frequencies.

Figure 6 presents 3D views of sprayed droplets, colored by their velocity, under both constant and pulsed voltage conditions at frequencies of 200 Hz, 800 Hz, and 1600 Hz. In the constant voltage case, both the bell cup and the control ring are maintained at constant –40kV, while pulsed voltage of -40 kV<sub>rms</sub> is applied to the bell cup, with the ring conductor maintained at a constant -40 kV. At 200 Hz (Fig. 6b), the longer intervals between voltage pulses allow more liquid to accumulate at the bell-cup edge before ejection. This results in the formation of larger droplets, which tend to follow irregular trajectories due to centrifugal forces, leading to poor directional uniformity. Consequently, droplet dispersion becomes inconsistent, increasing overspray and material loss. At 800 Hz (Fig. 6c), the voltage pulses occur more frequently, reducing liquid accumulation at the bell edge and producing smaller, more uniform droplets. These droplets follow more consistent paths under the influence of both centrifugal and electrostatic forces, resulting in improved spray precision, better coverage, and reduced overspray. At 1600 Hz (Fig. 6d), the droplets become even finer due to rapid pulsing. However, their smaller size makes them more sensitive to external disturbances such as ambient airflow, causing them to spread beyond the intended target area. Overall, increasing the pulsed voltage frequency leads to a more concentrated and uniform droplet size distribution. Both 800 Hz and 1600 Hz configurations provide better spray uniformity and reduced overspray compared to the constant voltage case.

In table 1, the overall transfer efficiency (TE) is reported for the different cases studied. TE is calculated as:  $TE = (m_f - m_i) \times 100/m_{out}$ , where  $m_f$  is the mass after painting,  $m_i$  is the initial mass, and  $m_{out}$  is the mass of paint emitted from the nozzle. Under constant -40 kV voltage, TE reaches 79.1%. With pulsed voltage at -40 kV<sub>rms</sub> on the sprayer's bell cup, TE is 77.1% at 200 Hz, slightly lower than the constant voltage case; TE increases at higher frequencies, reaching 84.3% at 800 Hz and 82.9% at 1600 Hz, demonstrating improved performance at higher pulsed frequencies.

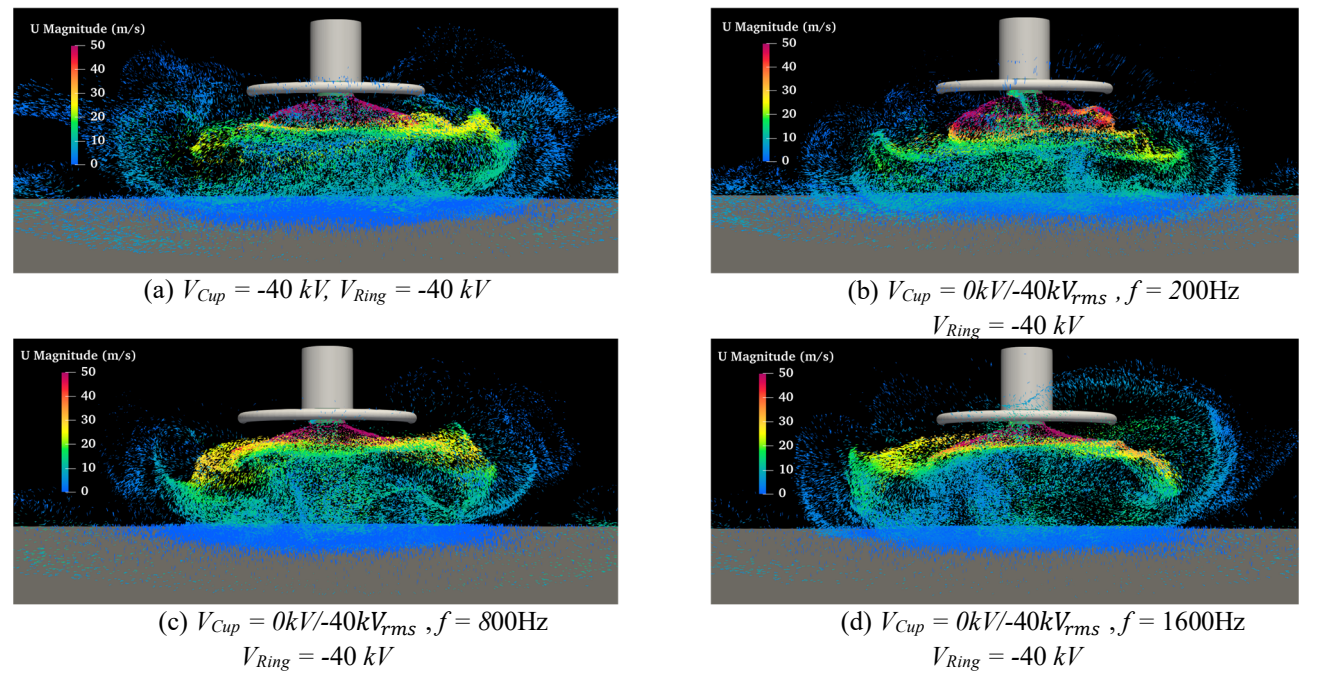


Fig. 6. Paint spray distribution pattern for ERBS under constant voltage  $(V_{Cup} = -40 \text{ kV}, V_{Ring} = -40 \text{ kV})$  and pulsed voltage applied to the sprayer's body cup  $(V_{Cup} = 0 \text{kV} / -40 \text{ kV}_{rms}, V_{Ring} = -40 \text{ kV})$  at different frequencies.

Table 1. Transfer efficiency (TE) for different conditions ( $\omega_{Bell} = 30kRPM, \rho_m^q = -0.5 \ mC/kg$ ).

Applied voltage	Frequency (Hz)	Transfer efficiency (TE)%
Constant voltage	-	79.1
$V_{Cup} = -40 \ kV, \ V_{Ring} = -40 \ kV$		
Pulsed voltage on the cup	200	77.1
$V_{Ring} = -40 \ kV, \ V_{Cup} = 0kV / -40kV_{rms}$	800	84.3
	1600	82.9

## 5. Conclusion

In this study, we investigated the effect of using pulsed high voltage in ERBS electrostatic spray using a 3D Eulerian-Lagrangian framework in OpenFOAM incorporating a Large Eddy Simulation (LES) turbulence model along with spray dynamics, electric field modeling, and droplet tracking. The results showed that under a constant voltage of -40 kV, the transfer efficiency (TE) was 79.1%. When applying pulsed voltage at -40 kV $_{\rm rms}$  to the sprayer's body cup, TE was slightly lower at 200 Hz (77.1%), but improved significantly at higher frequencies—peaking at 84.3% at 800 Hz and reaching 82.9% at 1600 Hz. These findings suggest that pulsed voltage, especially at higher frequencies, can enhance spraying performance compared to constant voltage operation.

## **Acknowledgements**

This study was supported by GreenAuto Project: Green Innovation for the Automotive Industry, n° 02/C05-i01.02/2022.PC644867037-00000013 from the Incentive System to Mobilizing Agendas for Business Innovation, funded through the Recovery and Resilience Plan. It was also supported by the Portuguese Foundation for Science and Technology, I.P. (FCT, I.P.) FCT/MCTES through national funds (PIDDAC), under the R&D Unit C-MAST, Center for Mechanical and Aerospace Science and Technologies, Research Unit No. 151, reference: Projects UIDB/00151/2020 (https://doi.org/10.54499/UIDB/00151/2020) and UIDP/00151/2020 (https://doi.org/10.54499/UIDP/00151/2020).

## References

- [1] Y. Matsushita, T. Katayama, Y. Saito, Y. Matsukawa, T. Okabe, M. Shirota, T. Inamura, M. Daikoku, J. Fukuno and H. Aoki, H, "A spray painting simulation using high-speed rotary Atomizer—Model development and comparison of LES and RANS—," *Results in Engineering*, 21, p.101697, 2024.
- [2] V. Viti and J. Kulkarni, "CFD analysis of the electrostatic spray-painting process with a rotating bell cup," In: *ILASS Americas*, 21st Annual Conference on Liquid Atomization and Spray Systems, Orlando, Florida, USA, 2008.
- [3] A. Darwish Ahmad, A. M. Abubaker, A. A. Salaimeh, and N. K. Akafuah, "Schlieren visualization of shaping air during operation of an electrostatic rotary bell sprayer: Impact of shaping air on droplet atomization and transport," *Coatings*, 8(8):279, 2018.
- [4] C. Stevenin, Y. Bereaux, J. Y. Charmeau, and J. Balcaen, "Shaping airflow characteristics of a high-speed rotary-bell sprayer for automotive painting processes," *Journal of Fluids Engineering*, 137(11):111304, 2015.
- [5] K. S. Im, M. C. Lai, S. T. J. Yu, and R. R. Matheson, "Simulation of spray transfer processes in electrostatic rotary bell sprayer," *Journal of Fluids Engineering*, 126:449-456, 2004.
- [6] K. Yasumura, Y. Saito, M. Shoji, Y. Matsushita, H. Aoki, T. Miura, S. Ogasawara, M. Daikoku, M. Shirota, T. Inamura, "A numerical investigation of the factor decreasing transfer efficiency in a high-speed rotary bell-cup atomizer," *Kagaku Kogaku Ronbunshu* 37,251–260, 2011
- [7] M. R. Pendar and J. C. Páscoa, "Numerical analysis of charged droplets size distribution in the electrostatic coating process: Effect of different operational conditions," *Physics of Fluids*, 33(3):033317, 2021.
- [8] M. R. Pendar, S. Cândido, and J. C. Páscoa, "Optimization of painting efficiency applying unique techniques of high-voltage conductors and nitrotherm spray: Developing deep learning models using computational fluid dynamics dataset," *Physics of Fluids*, 35(7), 2023.
- [9] S. A. Colbert and R. A. Cairncross, "A computer simulation for predicting electrostatic spray coating patterns," *Powder Technology*, 151:77-86, 2005.
- [10] V. Krisshna, W. Liu, and M. Owkes, "High-fidelity simulations of a rotary bell atomizer with electrohydrodynamic effects," *International Journal of Multiphase Flow*, 168:104566, 2023.
- [11] N. Toljic, K. Adamiak, G.S.P. Castle, H.-H. Kuo, H.-T. Fan, "3D numerical model of the electrostatic coating process with moving objects using a moving mesh," *J. Electrost.* 70, 499–504, 2012.
- [12] W. Oswald, L. Geodeke, P. Ehrhard, and N. Willenbacher, "Influence of the elongational flow resistance and pigmentation of coating fluids on high-speed rotary bell atomization," *Atomization and Sprays*, 29(10):913, 2019.
- [13] B. Shen, Q. Ye, N. Guettler, O. Tiedje, and J. Domnick, "Primary breakup of a non-Newtonian liquid using a high-speed rotary bell atomizer for spray painting processes," *Journal of Coatings Technology and Research*, 16(6):1581–1596, 2019.
- [14] A. Benmoussa, L. Rahmani, and B. Draoui, "Simulation of Viscoplastic Flows in a rotating Vessel Using a Regularized Model," *The International Journal of Multiphysics*, 11(4), 349-358, 2017.
- [15] L. Rahmani, O. Seghier, A. Benmoussa and B. Draoui, "CFD study of the thermal transfer of a non-Newtonian fluid within a tank mechanically stirred by an anchor-shaped impeller". In EPJ Web of Conferences, 180, 02089, 2018. EDP Sciences.
- [16] V. Krisshna, and M. Owkes, "Investigating atomization characteristics in an electrostatic rotary bell atomizer," *International Journal of Multiphase Flow*, 175, p.104814, 2024.
- [17] S. Cândido, and J. C. Páscoa, "Data-driven surrogate modelling of multistage Taylor cone–jet dynamics," *Physics of Fluids*, 36(5), 2024.
- [18] A. Benmoussa, M. R. Pendar, and J. C. Páscoa, J. C, "Enhancing electrostatic spray-painting efficiency with modified high-voltage conductors: A numerical study on pulsed electric fields," *Journal of Aerosol Science*, 184, 106491, 2025.
- [19] M. R. Pendar and J. C. Páscoa, "Atomization and spray characteristics around an ERBS using various operational models and conditions: numerical investigation," *International Journal of Heat and Mass Transfer*, 161, 120243, 2020.
- [20] S. Laín and C. A. Grillo, "Comparison of turbulent particle dispersion models in turbulent shear flows," *Brazilian Journal of Chemical Engineering*, 24:351-363, 2007.